APPLIED PHYSICS

From the generalized reflection law to the realization of perfect anomalous reflectors

Ana Díaz-Rubio,* Viktar S. Asadchy, Amr Elsakka, Sergei A. Tretyakov

The use of the generalized Snell's law opens wide possibilities for the manipulation of transmitted and reflected wavefronts. However, known structures designed to shape reflection wavefronts suffer from significant parasitic reflections in undesired directions. We explore the limitations of the existing solutions for the design of passive planar reflectors and demonstrate that strongly nonlocal response is required for perfect performance. A new paradigm for the design of perfect reflectors based on energy surface channeling is introduced. We realize and experimentally verify a perfect design of an anomalously reflective surface using an array of rectangular metal patches backed by a metallic plate. This conceptually new mechanism for wavefront manipulation allows the design of thin perfect reflectors, offering a versatile design method applicable to other scenarios, such as focusing reflectors, surface wave manipulations, or metasurface holograms, extendable to other frequencies.

INTRODUCTION

The classical approach to design of wave-shaping reflectors for light or microwave radiation is based on geometrical optics. A flat mirror obviously obeys the usual reflection law: In the absence of dissipation, all reflected rays go in the specular direction (the incidence and reflection angles are equal, $\theta_i = \theta_r$) without changing the field amplitude. The distribution of reflected field intensity can be engineered by shaping the reflecting surface. Because of the differences in ray propagation path lengths, the phase distribution at the reflector aperture can be tuned so that, for example, all rays converge at a point, forming a focal spot. Generalizing the phased-array antenna principle, the same function can be realized in a planar reflector if the reflection phase is made nonuniform over the reflector surface. In antenna applications, these nonuniform reflectors are called reflectarrays and are usually realized as arrays of resonant antennas (1). Most commonly, patch antennas are used and the reflection phase from every element is tuned either by reactive loads or by varying patch size or shape. Reflectarrays with subwavelength distances between the array elements are called high-impedance surfaces (2, 3) or metasurfaces (4).

We consider the anomalous reflection scenario illustrated in Fig. 1A. According to the phased-array principle, to reflect an incident plane wave into another plane wave, breaking the usual reflection law (the reflection angle $\theta_r \neq \theta_i$), the reflection phase should depend linearly on the corresponding coordinate along the reflector plane. In this situation, one can expect that reflections from all the points interfere constructively in a plane wave propagating in the desired direction. Recently, this simple design principle was formulated in the form of the "generalized Snell's law" (5). To understand this law, let us assume that a plane wave is incident at a planar reflecting surface at the incidence angle θ_i and introduce a Cartesian coordinate system with the x axis along the projection of the wave vector to the reflector plane. If the reflected plane wave is propagating at the reflection angle θ_r and its amplitude is the same as in the incident wave, then the ratio of the tangential electric fields in the reflected wave and in the incident wave at the reflector surface is given by $\exp(j\Phi_r) = \exp[j(\sin\theta_i - \sin\theta_r)k_1 x]$. Here, $k_1 = \omega\sqrt{\mu\varepsilon}$ is the wave number in the background isotropic medium, and we assume the time-harmonic dependency $e^{j\omega t}$. The local reflection

coefficient $R = (Z_s(x) - \eta_1)/(Z_s(x) + \eta_1) = \exp(j\Phi_r)$, where η_1 is the wave impedance of the incident plane wave (ratio between the tangential components of the electric and magnetic fields), defines a periodically modulated boundary surface. The surface impedance $Z_s(x)$, defined as the ratio between the tangential components of the total electric and magnetic fields (incident and scattered) at the surface, is purely imaginary and can be expressed as

$$Z_s(x) = j\frac{\eta_1}{\cos\theta_i}\cot[\Phi_r(x)/2] \tag{1}$$

Equation 1 is a well-known solution that has been used in numerous studies (6–13). Nevertheless, the sum of the incident and one reflected plane wave is not a valid solution for the Maxwell equations with the surface impedance given by Eq. 1. This means that when we illuminate a metasurface characterized by surface impedance (Eq. 1) given by the generalized reflection law with a plane wave at θ_i, in addition to the desired anomalously reflected plane wave at θ_r, more plane waves will be excited in the system to satisfy the power conservation and the boundary conditions, leading to parasitic reflections or energy absorption in the reflector (14, 15).

Figure 1B shows the numerical estimate of the efficiency (the ratio between the power sent into the desired direction and the incident power) for a metasurface based on the generalized Snell's law modeled by the impedance boundary as in Eq. 1. We can see that in all known realizations, the power efficiency is lower than the numerical prediction due to imperfections in fabrication and discretization problems. It is also worth noting that the efficiency markedly decreases when the desired reflection angle deviates more and more from the specular reflection angle. At optical frequencies, traditional diffraction gratings are periodic surfaces engineered for controlling the percentage of energy reflected into each diffraction mode. In principle, for a certain incidence angle θ_i, the surface profile can be tailored to send the energy into some reflection angle θ_r. These devices work efficiently for retroreflection ($\theta_i = -\theta_r$) or with small differences between the incidence and reflection directions ($\theta_i \approx -\theta_r$) (16, 17), but the efficiency decreases when the difference between the incidence and reflection angles increases.

Let us look into this important feature in more detail. The period of the metasurface D_x is defined by requiring that the reflection phase is 2π-periodic: $\Phi_r(x) = \Phi_r(x + D_x) + 2\pi$, and considering the phase shift in reflection dictated by the generalized Snell's law, it can be expressed as

Department of Electronics and Nanoengineering, Aalto University, P.O. Box 15500, FI-00076 Aalto, Finland.
*Corresponding author. Email: ana.diazrubio@aalto.fi
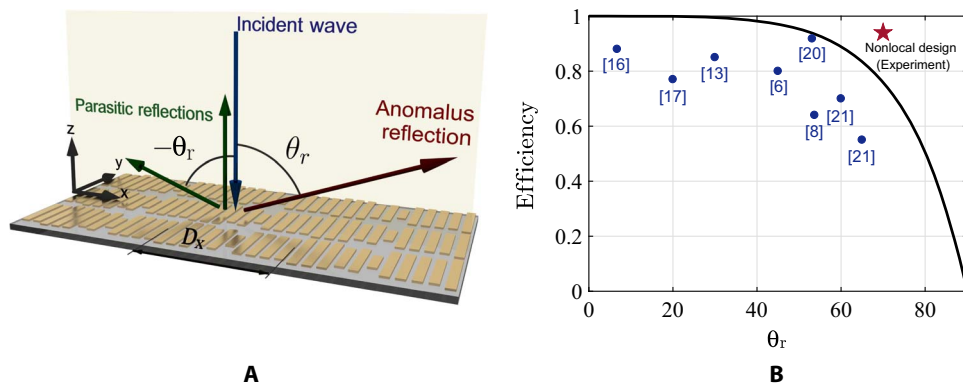
Fig. 1. Anomalous reflective metasurface. (**A**) Illustration of the performance of a reflective metasurface. Propagating waves in the system when $\theta_i = 0°$ and $\theta_r > 30°$ are represented in the scheme. (**B**) Comparative overview of the efficiency of anomalous reflection metasurfaces and optical gratings. Blue dots represent previous results found in the literature (6, 8, 13, 16, 17, 20, 21); the black line represents the numerical estimation of the designs based on a linear 2π phase gradient calculated according to Eq. 1; the red star represents the results obtained in this paper.

$D_x = \lambda/|\sin \theta_r - \sin \theta_i|$, where $\lambda = 2\pi/k_1$ is the wavelength. The period will define the directions where the reflected energy can flow. For example, considering normal incidence, $\theta_i = 0°$ and $\theta_r > 30°$, the energy can only be reflected as plane waves in three different directions (Fig. 1A): the specular direction (θ_i), the desired direction (θ_r), and the symmetric direction ($-\theta_r$). Numerical simulations have been done modeling a metasurface with the impedance boundary described by Eq. 1. In particular, the impedance boundary has been designed to reflect the energy from $\theta_i = 0°$ to $\theta_r = 70°$. Figure 2A shows the distribution of the real part of the scattered electric field, where we see an interference pattern produced by these three plane waves. As previously stated, the energy is distributed into three directions, producing a modulation of the real part of the Poynting vector, as shown in Fig. 2D. It is important to notice that the amplitude of the reflected wave in the desired direction is higher than the incident amplitude, $E_r/E_i = 1.5$, so the metasurface not only is adding a linear phase shift as it was expected but also changes the amplitude. This property agrees with the conclusion that more than two propagating plane waves must exist in the system. The efficiency of this conventional design is $\xi_P = P_r/P_i = 0.76$, and the residuary energy is sent to the other directions. In this definition of the power efficiency, P_r and P_i are the amplitudes of the Poynting vector of the plane wave reflected in the desired direction and that of the incident plane wave, respectively.

Parasitic reflections can be suppressed by allowing power absorption in the metasurface. As shown by Asadchy *et al.* (14) and Estakhri and Alù (15), a solution for the Maxwell equations, where $E_r = E_i$, can be found and the corresponding surface impedance [for transverse electric (TE)–polarized waves] reads

$$Z_s(x) = \eta_1 \frac{1 + e^{j\Phi_r(x)}}{\cos \theta_i - \cos \theta_r e^{j\Phi_r(x)}} \quad (2)$$

The impedance given by Eq. 2 is a complex number with some positive real part and the same period as in the conventional design (Eq. 1). The real part in the surface impedance represents losses in the metasurface. Figure 2 shows the results of numerical simulations of a metasurface defined by Eq. 2 when $\theta_i = 0°$ and $\theta_r = 70°$. The real part of the scattered field is represented in Fig. 2B. We can see that a perfect plane wave with the same amplitude as the incident wave is reflected into the

desired direction. The real part of the Poynting vector is represented in Fig. 2E, where we can see the power entering into the metasurface due to nonzero values of the real part of the impedance (the metasurface is lossy). The efficiency of this metasurface is $\xi_P = P_r/P_i = 0.34$, and the absorption is $A = 1 - P_r/P_i = 0.66$. Figure 2E shows that the magnitude of the power is modulated in the x-z plane with a flat wavefront. From the comparison between the spatial distributions of the electric field and the Poynting vector, it is easy to see that the tilt angle defining this modulation, θ_{power}, is different from the direction of the reflected wave phase front, θ_r. The reader is referred to the Supplementary Materials for more information.

Very recently, it was shown that it is, in principle, possible to realize anomalously reflecting metasurfaces that operate perfectly, that is, without any parasitic reflections, scattering, and absorption (14, 18). To achieve perfect anomalous reflection, the power carried in the desired direction must be equal to the power of the incident plane wave, so the amplitude of the reflected wave should be $E_r = E_i \frac{\sqrt{\cos \theta_i}}{\sqrt{\cos \theta_r}}$ (14). Considering this condition, the surface impedance can be written as

$$Z_s(x) = \frac{\eta_1}{\sqrt{\cos \theta_i \cos \theta_r}} \frac{\sqrt{\cos \theta_r} + \sqrt{\cos \theta_i}\, e^{j\Phi_r(x)}}{\sqrt{\cos \theta_i} - \sqrt{\cos \theta_r}\, e^{j\Phi_r(x)}} \quad (3)$$

The analysis of this expression shows that the input impedance is a complex number, whose period is equal to the conventional design (Eq. 1) and the lossy design (Eq. 2). The real part of the input impedance periodically takes positive (corresponding to loss) and negative (gain) values. The power that passes through the input surface in the "lossy" regions is reradiated from the "active" regions so that the overall metasurface response is lossless. Figure 2 (C and F) shows the numerical simulations for this design when $\theta_i = 0°$ and $\theta_r = 70°$. The real part of the scattered electric field is represented in Fig. 2C. In this case, the ratio between the scattered and incident fields, $E_r/E_i = 1.7$, fulfils the condition for the power conservation previously mentioned, and the power efficiency equals 100%. Figure 2F shows the power flow where one can visualize this behavior. Actual implementations of these perfect anomalous reflectors can be done by using the following approaches: (i) including active and lossy elements in the metasurfaces (15), as it is
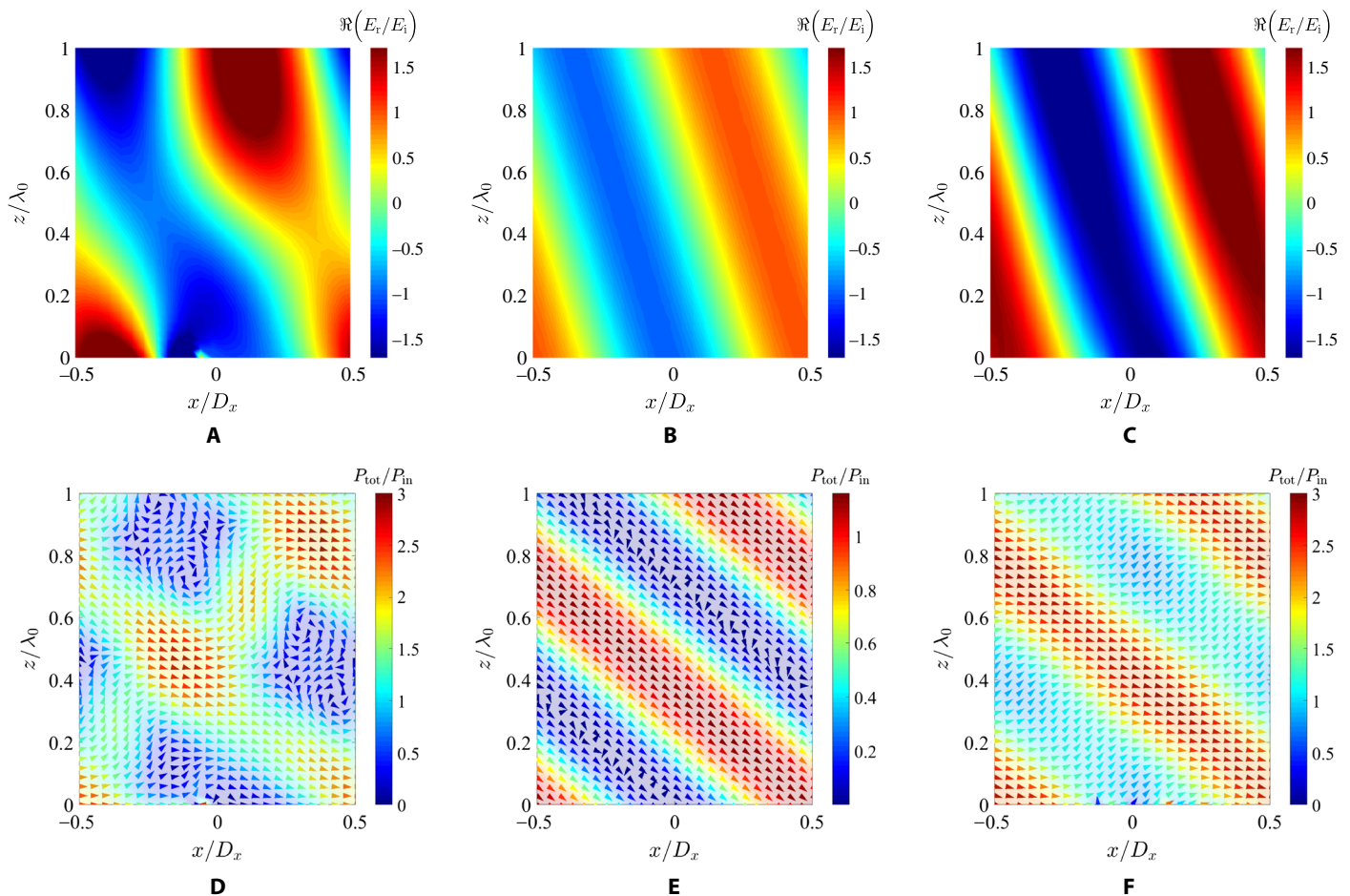
Fig. 2. Comparison between the different reflective metasurface proposals when θᵢ = 0° and θᵣ = 70°. Conventional design: Real part of the scattered electric field (**A**) and total power density distribution (**D**). Lossy design: Real part of the scattered electric field (**B**) and total power density distribution (**E**). Active design: Real part of the scattered electric field (**C**) and total power density distribution (**F**).

dictated by Eq. 3 (however, the use of active elements is usually not desirable for practical reasons and leads to potentially unstable structures); (ii) using auxiliary evanescent fields for avoiding the modulation of the normal component of the Poynting vector at the metasurface, as it was theoretically demonstrated by Epstein and Eleftheriades (18) for penetrable metasurfaces (metasurfaces allowing fields at both sides) (in these theoretical designs, by engineering the evanescent fields excited at the metasurface, one can ensure the local power conversation at each point of the metasurface); and (iii) creating passive but nonlocal metasurfaces and engineering the interactions between the constitutive elements (that is, the effects of evanescent fields generated in the array) to allow proper energy channeling along the metasurface. In this last scenario, the cell-averaged normal component of the Poynting vector equals to zero, whereas the local behavior appears either lossy or active.

Inspired by the physical principle of leaky-wave antennas, we introduce a new approach based on the modulation of the reactive impedance of the metasurface. We demonstrate that a perfect anomalous reflector can be realized as a simple metal pattern on a thin grounded dielectric slab. In this scenario, engineered modulations of the surface reactance ensure the required nonlocal reflections, which are eventually perfectly launched only in the desired direction. We present and clarify the main conceptual differences between local and nonlocal approaches

in the use of evanescent fields to realize perfect anomalous reflectors. On the basis of the developed theory, we design, manufacture, and experimentally study a metareflector prototype, which reflects a normally incident plane wave into a plane wave at the tilt angle θᵣ = 70°. The experimental results confirm that this first prototype of metasurfaces for perfect control of reflections operates according to expectations: The realized power efficiency is close to 100%, limited only by dissipation in the metal patches and the dielectric substrate. Parasitic reflections into the specular direction and other directions are seen to be negligible. The proposed simple topology allows cheap mass production manufacturing based on the conventional printed circuit board technology (microwave frequencies) or various lithography techniques (terahertz and beyond).

RESULTS

Theoretical local design of a lossless perfect anomalous reflector

First, we consider a surface impedance model of the metasurface and study the problem by using locally responding impedance boundaries. We propose that the most reasonable approach to obtain the impedance boundary, which realizes perfectly reflecting lossless reflectors, is to use

inhomogeneous leaky-wave surfaces, generalizing the concept of leaky-wave antennas. Leaky-wave antennas are formed by perturbed waveguides or transmission lines, naturally offering the needed channel for transporting power from receiving areas to transmitting areas. Even more importantly, tuning the inhomogeneity profiles along the antenna surface, it appears possible to realize regimes where the receiving areas receive power predominantly from the illumination direction while the radiating areas send the waves predominantly in the desired direction of anomalous reflection. Thus, tuning the phase synchronism of free-space waves and leaky waves on the surface, we can realize directive power transfer along the surface without using any nonreciprocal elements.

We start the study by considering the surface impedance model of a leaky-wave structure. Within this model, lossless reflectors are described by a reactive surface impedance, Z_{s0}. To allow propagation of a surface wave of the considered TE polarization along the surface, $E_y = E_0 e^{-j\beta_s x - \alpha z}$, we demand that the reactance is negative (capacitive) at every point of the surface $Z_{s0} = E_y/H_x = -j\omega\mu_0/\alpha$. The tangential wave number of the surface wave can be found using the relation $\beta_s^2 = k_1^2 + \alpha^2$. Thus, the tangential wave number can be written as

$$\beta_s = k_1 \sqrt{1 - \frac{\eta_1^2}{Z_{s0}^2}} \tag{4}$$

To couple the surface wave to free space, the reactance should be nonuniform over the reflector surface. In conventional leaky-wave antennas, where the goal is to launch a wave in a specific direction, the surface is periodically perturbed. This perturbation generates spatial harmonics, whose tangential wave number can be expressed as

$$\beta_n = \beta_s + n\frac{2\pi}{D_x} \tag{5}$$

where $n = \pm 1, \pm 2, \ldots$. The corresponding vertical wave number, k_{zn}, can be found using

$$k_{zn} = \sqrt{k_1^2 - \beta_n^2} \tag{6}$$

Knowing the vertical and tangential wave numbers, the direction of the propagating waves is calculated using

$$\sin\theta_n = \frac{\beta_n}{k_1} = \sqrt{1 - \frac{\eta_1^2}{Z_{s0}^2}} + n\sin\theta_r \tag{7}$$

Panels B and C of Fig. 3 represent the tangential and vertical wave numbers, respectively, for different values of the surface impedance $Z_{s0} = jX_{s0}$.
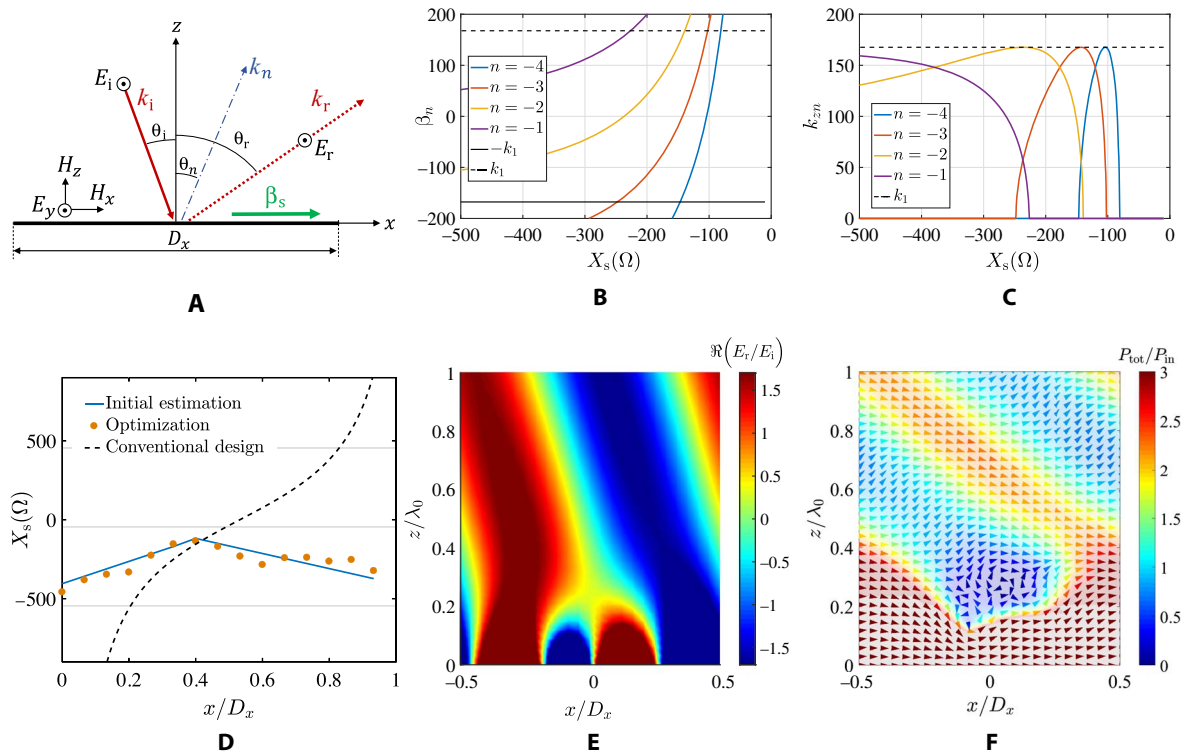
Fig. 3. Local design of a lossless perfect anomalous reflector. (**A**) Schematic representation of the proposed design methodology for the perfect reflecting metasurface based on the leaky-wave antenna behavior with a modulation in the impedance profile. Tangential (**B**) and vertical (**C**) wave numbers introduced in the system due to a periodic perturbation with period $D_x = \lambda/|\sin\theta_i - \sin\theta_r|$ as a function of the surface impedance $Z_s = jX_s$. (**D**) Surface impedance of the metasurface when $\theta_r = 70°$ and $\theta_i = 0°$. Blue line represents the initial estimation of the surface reactance (Eq. 11), and orange dots represent the optimized values of the surface reactance on the discretized surface. Dashed line represents the impedance of conventional design described by Eq. 1. Numerical results of a perfect reflectarray based on the linearly modulated leaky-wave antenna structure: Real part of the scattered electric field (**E**) and total power density flow distribution (**F**).

The impedance surface should be chosen to couple the energy to free space through leaky waves. For example, if we choose $X_{s0} = -124\ \Omega$, only the harmonics $n = -3$ and $n = -4$ propagate in free space. In particular, for $X_{s0} = -124\ \Omega$, the waves propagate in the directions specified by $\theta_{-3} = 22.3°$ and $\theta_{-4} = -34°$. Once we have determined the surface impedance that allows surface wave propagation and coupling with free-space waves, the reactance should be modulated. Conventional periodical modulations (usually with a sinusoidal profile) provide coupling to the waves along these two directions (in this example). But as we saw above, to realize perfect anomalous reflection, in the areas where the surface should receive power from the incident field, the wave along the surface should be in phase synchronism with the incident plane wave. In contrast, in the areas where the energy should be launched into the desired direction, the synchronization should hold for the reflected plane wave.

To realize this operation, we propose to modulate the reflection phase linearly using the generalized reflection law separately for these two parts of the metasurface period. The required derivative of the local phase can be estimated by considering the additional effective "momentum" along the surface, in analogy with the generalized law of reflection. The required linear phase dependence can be written as

$$
\Phi_r(x) = \begin{cases} \Delta\theta_r\, k_1 x - \Phi_0 & 0 \le x < x_1 \\ \Delta\theta_i\, k_1 (x - D_x) - \Phi_0 & x_1 \le x < D_x \end{cases} \quad (8)
$$

where $\Delta\theta_r = \sin\theta_r - \sin\theta_n$ and $\Delta\theta_i = \sin\theta_i - \sin\theta_n$. In our particular example, the derivative has the opposite sign in the two parts of the surface period (shifting the angle $\theta_{-3} = 22.3°$ to zero and $70°$, respectively), and $x_1 = D_x \frac{\sin\theta_n - \sin\theta_i}{\sin\theta_r - \sin\theta_i}$ is the point where the derivative of the reflection phase changes from positive to negative. The initial phase shift reads

$$
\Phi_0 = 2\pi \frac{(\sin\theta_r - \sin\theta_n)(\sin\theta_n - \sin\theta_i)}{(\sin\theta_r - \sin\theta_i)^2} - 2\arctan\frac{X_{s0}}{\eta_1} \quad (9)
$$

Notice that $\Phi_r(x_1) = 2\arctan\frac{X_{s0}}{\eta_1}$ corresponds to the phase of the reflection coefficient for the homogeneous surface impedance $Z_{s0} = jX_{s0}$. The relation between the phase gradient and the modulated surface impedance can be found through the reflection coefficient

$$
\Phi_r(x) = 2\arctan\frac{X_s(x)}{\eta_1} \approx 2\frac{X_s(x)}{\eta_1} \quad (10)
$$

where the approximation holds for small values of X_s/η_1. Using Eq. 10, we can estimate the modulations needed for the metasurface input impedance using the following expression

$$
X_s(x) = \begin{cases} \dfrac{\eta_1}{2}\left(k_1 \Delta\theta_r\, x - \Phi_0\right) & 0 \le x < x_1 \\ \dfrac{\eta_1}{2}\left(k_1 \Delta\theta_i\, (x - D_x) - \Phi_0\right) & x_1 \le x < D_x \end{cases} \quad (11)
$$

The blue line in Fig. 3D represents the surface reactance profile defined by Eq. 11 when $X_{s0} = -124\ \Omega$, $n = -3$, $\theta_i = 0°$, and $\theta_r = 70°$. Obviously, this analytical estimation of the perfect reactance profile is rather approximate, because we make use of the homogeneous reactance model in case when the assumption that the metasurface is uniform on the wavelength scale is not properly justified. For this reason, we then perform numerical optimization of the surface reactance, setting these estimations of the required reactance profile as the initial guess and using 15 elements for the discretization as a piecewise homogeneous reactive impedance boundary. As a result, we find the profile shown in Fig. 3D with the red dots (one dot corresponds to one homogeneous reactive surface element). As expected from the above theory, it is everywhere capacitive, growing in one half of the period and decaying inside the other half. The differences with the analytically predicted values are due to the approximations in the models and are caused mainly because of the periodic conditions imposed over the unit cell and the piecewise constant numerical model of the surface that force generation of more complex evanescent field structure than assumed in the analytical analysis.

Numerical simulations of the corresponding field and the Poynting vector distributions are shown in Fig. 3 (E and F). We see that a surface wave propagating along the surface is formed. If we now define a reference plane above the volume filled by the surface mode fields (which is our "input port" to the metasurface structure) and look at the input impedance there, we see that it satisfies the requirements of perfect operation: It is a complex value given by Eq. 3, and the real part is properly varying, emulating "loss" where the power is received by the leaky-wave structure and "gain" in the areas where it is launched back.

Table 1 summarizes the field amplitudes and the power sent into the three directions (θ_i, θ_r, $-\theta_r$) when the metasurface is illuminated by a normally incident plane wave for the different design options. It is clear that the inhomogeneous leaky-wave antenna design promises perfect performance.

To complete the study of this metasurface, we consider the frequency bandwidth (Fig. 4A) and give a comparison with the conventional

Table 1. Numerical results and comparison between the different design possibilities for reflectarrays. Amplitude/power of waves sent into the respective directions, absorption coefficient, and power efficiency.

	θ_i	θ_r	$-\theta_r$	Absorption	Efficiency
Generalized reflection law (Eq. 1)	0.24/0.06	1.50/0.76	0.73/0.18	0.00	75.7%
Lossy design dictated by Eq. 2	0.00/0.00	1.00/0.34	0.00/0.00	0.66	34.0%
Active-lossy design dictated by Eq. 3	0.03/0.00	1.77/1.04	0.11/0.00	0.00	104.4%
Inhomogeneous leaky-wave antennas introduced in this paper	0.04/0.00	1.70/0.99	0.03/0.00	0.00	99.7%
Implementation with metal patches (lossy materials)	0.04/0.00	1.66/0.94	0.03/0.00	0.06	94.0%

designs (Fig. 4B). In both cases, below 7.5 GHz, no diffracted modes are allowed in the system, and consequently, all the energy is reflected back in the normal direction. In the range of frequencies between 7.5 and 9 GHz, the behavior of the two designs is different. At these frequencies, three diffraction modes are allowed ($n = 0, \pm 1$), and the efficiency of each mode, ξ_n, is calculated as the ratio between the power reflected into the nth mode and the incident power. The values at 8 GHz correspond to the values reported in Table 1. The conventional design based on a 2π linear phase gradient along the period shows a broadband response in the assumption that Eq. 1 is exactly satisfied at all frequencies (Fig. 4A). The efficiency of the $n = 1$ mode increases because of a reduction of the reflection angle. Considering the relation between the frequency and the reflection angle, this behavior is similar to a dispersive prism where waves of different frequencies are sent into different directions (movie S1). On the other hand, the design based on the inhomogeneous leaky-wave antenna shows a completely different behavior (Fig. 4B). In this case, the anomalous reflection is a relatively narrow-band phenomena ($\xi_1 > 0.5$ from 7.9 to 8.09 GHz), and the metasurface acts as a mirror for other frequencies. This feature can be useful for narrow filtering or monochromatic emitters. It is important to notice that, in both scenarios, the model assumes that the boundaries are not dispersive with respect to the frequency or the incidence angle. Thus, the frequency dispersion of the response is caused only by the properties of the phase gradient. In any physical implementation, the response will be modified because of the frequency and spatial dispersion of the meta-surface structure.

Figure 4 (C and D) compares the angular bandwidth of both designs (that is, the power sent in each diffracted mode as a function of the incidence angle). Here, the incidence angle varies from −40° to 40°. In this range, there are three different regions: from −3.5° to 3.5°, where three diffraction modes are allowed ($n = 0, \pm 1$); from −40° to −3.5°, with only two diffracted modes ($n = 0, 1$); and from 3.5° to 40°, also with two diffraction modes ($n = 0, -1$). Similar to the results for the frequency response, the behaviors of the two designs are completely different. The design introduced in this work has a sharp response with respect to the angle, and the anomalous reflection only appears for ± 2° around the normal incidence, whereas the surface behaves as a mirror for other incidence angles. However, in the conventional design, power is always coupled to $n = \pm 1$ modes, and the amount of power reflected in the specular direction is small. The maximum efficiency of this design is achieved at $\theta_i = \pm 28°$. The reflection angle can be calculated as $\theta_r = \arcsin(\sin \theta_i + n\sin 70°) = \mp 28°$. This particular case corresponds to the retroreflection scenario, where all the energy is sent back in the direction of the incident plane wave. It is also worth noting that retro-reflection is the only scenario where the interaction between the two existing plane waves does not produce power modulation, and the conventional linear phase gradient produces perfect results.

To summarize this section, we can conclude that the physics behind each of these designs is completely different, and consequently, that the potential applications for each will also be different. In terms of the frequency bandwidth and sensitivity to the incidence angle, conventional designs based on the generalized reflection law lead to comparably more broadband devices. On the other hand, devices that allow perfect anomalous reflection and transmission allow less frequency bandwidth and are more sensitive to variations of the incidence angle. This means that the applicability of nonlocal designs is limited to scenarios where the anomalous reflection is required for fields with a well-defined spatial spectrum, or high angular sensitivity is desirable for the device operation.
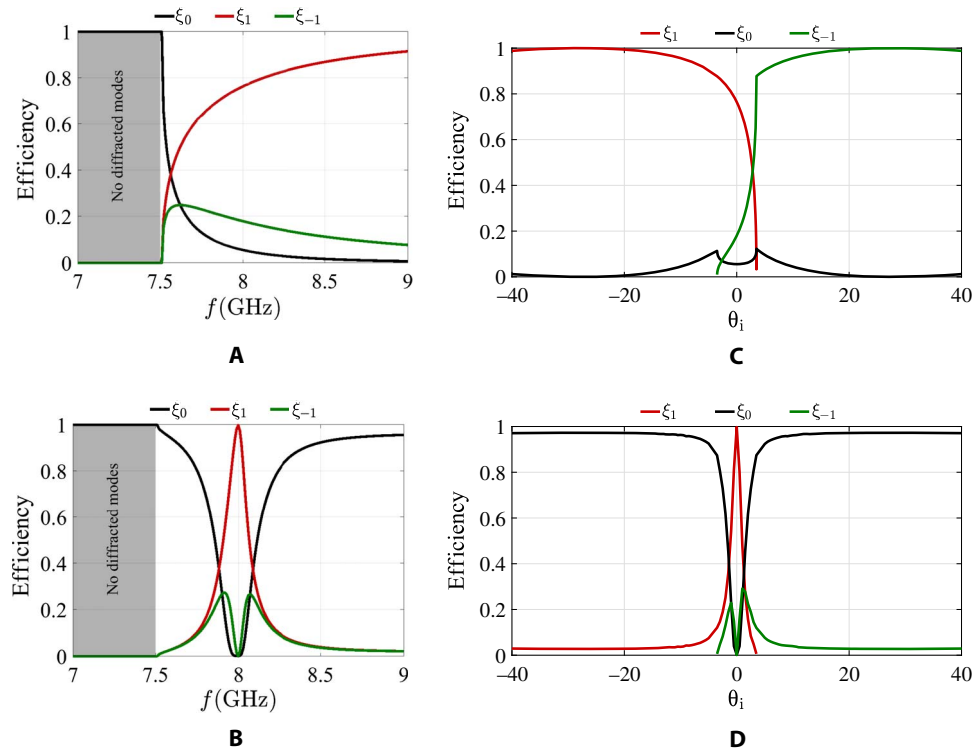
Fig. 4. Bandwidth analysis. Bandwidth comparison between anomalous reflectors based on (**A** and **C**) conventional design (Eq. 1) and on (**B** and **D**) inhomogeneous leaky-wave antenna (see Fig. 3D). Both metasurfaces are designed to produce anomalous reflection from 0° to 70° at 8 GHz and modeled as an inhomogeneous impedance boundary. (A and B) Comparison between wavelength bandwidths. (C and D) Comparison between angular bandwidths.

It is also important to notice the differences between conventional metasurfaces based on a linear phase gradient and inhomogeneous leaky-wave metasurfaces in terms of the implementation technique used for the actual designs. Conventional designs have shown that it is possible to implement the local impedance profile using nonlocal elements (for example, grooves in metal plates). However, in any actual realization of an inhomogeneous leaky-wave metasurface where the performance strongly depends on the reactive near fields (Fig. 3E), the existence of additional reactive fields due to the nonlocal behavior of the array elements will complicate the implementation difficult. That is, the design techniques used in the design of conventional metasurfaces do not ensure proper implementation of the impedance profile of leaky-wave metasurfaces, although the impedance that models the metasurface is local.
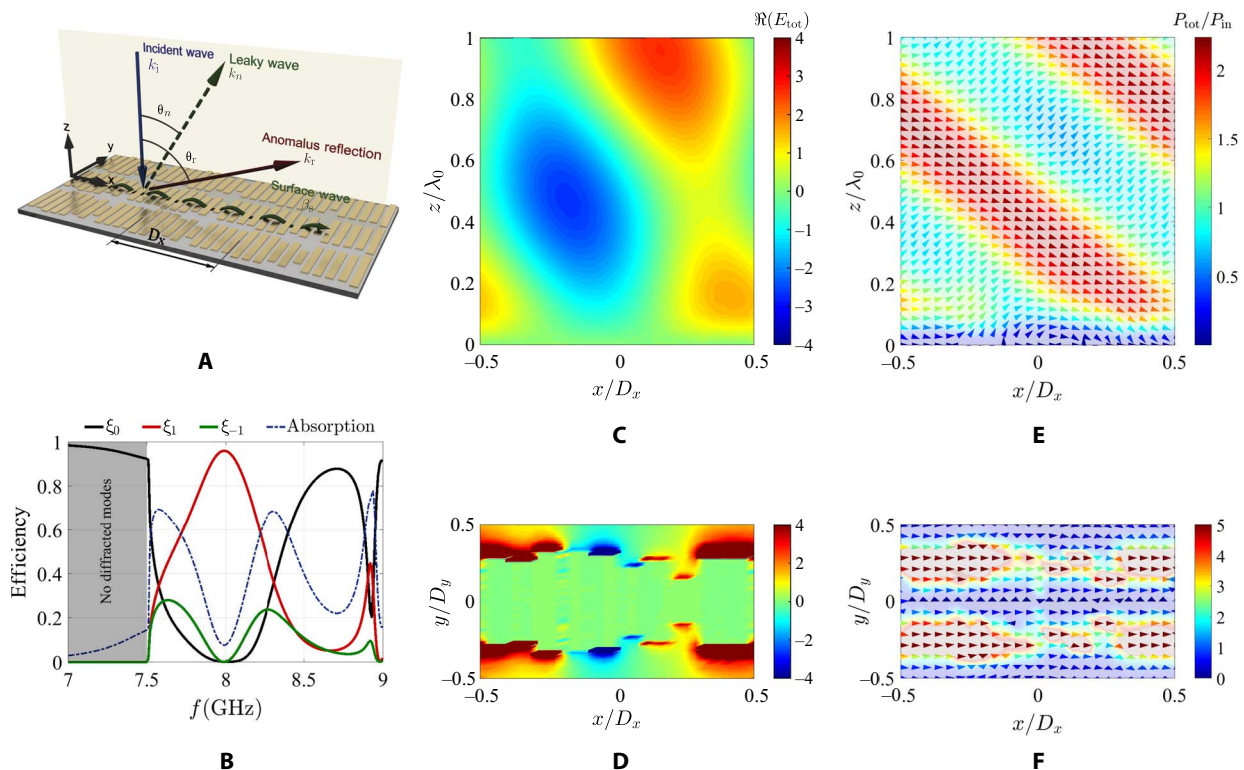
Nonlocal design, physical implementation, and experimental validations

The above results show the capability of surface waves propagating along an engineered gradient-phase metasurface to redirect energy and emulate the ideal "active-passive" behavior needed for the implementation of perfect reflectarrays. These results are based on the assumption that the metasurface behaves as a local impedance boundary, where no fields are allowed behind this boundary. Within this model, we can modify punctually one element of the metasurface without affecting the characteristics of the neighbors. However, this idealistic model does not provide guidelines for practical designs, because actual realizations of reactive surfaces require the use of some physical structures with a finite thickness so that there are fields behind the

mathematical metasurface boundary that couple the elements. In this case, the constituent elements cannot be designed individually using the model of periodical arrays of each element.

We approach the problem of realization of the required inhomogeneous leaky-wave surface by considering one of the simplest reactive impedance surfaces: a subwavelength array of metallic patches above a metal ground plane. A schematic representation of the proposed system is shown in Fig. 5A. The modulation of the field is done by changing the length of the patches. To obtain the proper response of the whole unit cell, we use a local estimation according to the phase gradient dictated by Eq. 3 as an initial guess (not considering the magnitude of the reflection coefficient) and carry out an optimization process for engineering the interactions between the elements and ensuring the desired nonlocal response of the surface. It is important to note that the optimization process does not aim to reproduce the local response illustrated in Fig. 3, whereas we aim to design the array of elements that will produce the overall "active-lossy" behavior described by Eq. 3. More information about the design process is available in Methods.

In particular, our design contains 10 metal patches per unit cell, all of them with the same width and centered along the $y = 0$ line (Fig. 5A). For the operational frequency of 8 GHz, the lengths of the patches are 10.7, 10.3, 12.3, 12, 11.8, 8.7, 10.2, 5.4, 11, and 10.9 mm. The patches are placed over a grounded dielectric slab with the permittivity $\epsilon_r = 2.2$ and the loss tangent $\tan \delta = 0.0009$. Figure 5 (C and E) shows numerical simulations of the electric field distribution of the designed metasurface. Figure 5D shows the simulated total Poynting vector distributions in the xz plane when $y = D_y/2$. The Poynting vector is distributed according to our predictions, the power is guided below the patches, and then it is

Fig. 5. Nonlocal implementation. (**A**) Proposed inhomogeneous nonlocal leaky-wave reflector. (**B**) Frequency bandwidth of the proposed design. Simulated real part of the total electric field (**C**) on the xz plane when $y = 0$ and (**D**) on the xy plane when $z = 0$. Real part of the total Poynting vector on (**E**) the xz plane when $y = D_y/2$ and real part of the Poynting vector (**F**) on the xy plane when $z = 0$.

launched into the desired direction. The power distribution in the plane that contains the patches is shown in Fig. 5F. We can see how the power is guided along the edges of the patches. An analysis of the evanescent fields that allow the energy channeling is available in the Supplementary Materials. Figure 5B shows the simulated frequency response. The behavior is similar to that of the local design (Fig. 4B), although the anomalous reflection frequency band is wider.

To experimentally verify the theory, we have designed and fabricated a reflectarray at 8 GHz (see Methods). We carried out three different experiments for the experimental validation. In the first experiment, the platform with the metasurface was rotating at an angle ϕ, whereas the positions of the antennas were fixed. Angle ϕ was counted from the line connecting the metasurface center and the transmitting antenna toward the normal to the metasurface plane (positive ϕ corresponded to the clockwise rotation of the platform when seen from the top). The signal reflected from the metasurface and measured by the receiving antenna $|S_{21,\mathrm{m}}|$ for different angles ϕ is shown in Fig. 6C. The experimental data were measured at the resonance of the metasurface occurring at 8.08 GHz.

The main peak of reflection toward the receiving antenna occurs when the metasurface is illuminated normally. This is an expected result, meaning that, in this case, most of the power impinging on the surface is reflected at 70° from the normal. The second peak occurring when $\phi = 35°$ corresponds to the specular reflection (incidence and reflection angles are equal) from the metamirror. These small nonzero specular reflections are acceptable because the metamirror was designed to have zero specular reflections only when illuminated normally.

To estimate the amplitude efficiency of the metasurface ξ_{r} ($\xi_{\mathrm{P}} = \xi_{\mathrm{r}}^2$), in the second experiment, we replaced the metasurface by an aluminum plate of the same size. The corresponding signal reflected from the plate

and measured by the receiving antenna $|S_{21,\mathrm{p}}|$ versus angle ϕ is shown in Fig. 6D. Now, the single peak of reflection occurs when the plate is illuminated at 35°, which corresponds to the specular reflection. To find the reflection efficiency of the metasurface, we normalize its signal amplitude $|S_{21,\mathrm{m}}|$ for $\phi = 0°$ by the signal amplitude from the reference uniform metal mirror $|S_{21,\mathrm{p}}|$ for $\phi = 35°$. We additionally divide the obtained value by the correction factor $\xi_0 = |S_{21,0\mathrm{m}}|/|S_{21,0\mathrm{p}}|$, which gives the ratio between the theoretically calculated signal amplitudes from an ideal metasurface (of the same size and made of lossless materials) and a perfect conductor plate. The correction factor ξ_0 is less than unity because, in this scenario, the radiating effective area of the perfect conductor plate is greater than that of the ideal reflecting metasurface due to a different orientation with respect to the antennas. At a frequency of 8.08 GHz in our particular configuration, the correction factor is equal to $\xi_0 = -2.41$ dB (see the Supplementary Materials). Thus, the reflection efficiency of the metasurface is calculated as

$$\xi_{\mathrm{r}} = \frac{1}{\xi_0} \frac{|S_{21,\mathrm{m}}(\phi = 0°)|}{|S_{21,\mathrm{p}}(\phi = 35°)|} = -0.28 \text{ dB} \qquad (12)$$

In the linear scale and expressed in terms of power, the reflection efficiency reaches 93.8%. This result is in excellent agreement with the 94% efficiency obtained using numerical solver (Table 1). The remaining 6.2% of power incident on the metasurface is mainly absorbed by it.

In the third measurement, we fixed the orientation of the metasurface at $\phi = 0°$ and used the transmitting antenna (fixed at the same position as in previous measurements) as both the transmitter and receiver. Using conventional time-gating post-processing procedure, we
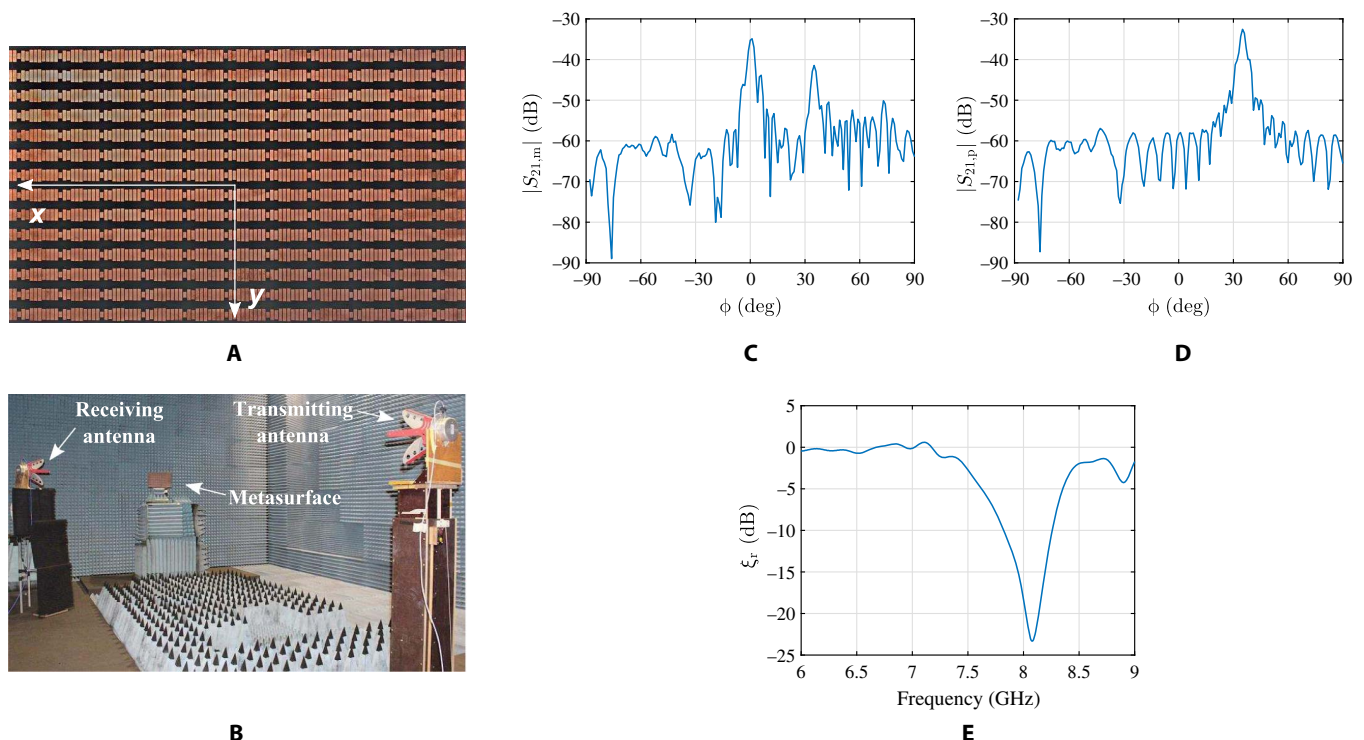
Fig. 6. Experimental verification. (**A**) Fabricated metasurface. (**B**) Experimental setup in an anechoic chamber. Signals measured by the receiving antenna for different orientation angles φ of (**C**) the metasurface and (**D**) the metal plate of equal size. (**E**) Amplitude efficiency of the metasurface illuminated normally.

could filter out all parasitic reflections received by the antenna (from the walls, absorbers, and due to the impedance mismatch between the antenna and the cables), retaining only the signal reflected from the metasurface. The measured signal amplitude was normalized by the corresponding amplitude from the reference uniform aluminum plate, which was measured likewise. This ratio, plotted in Fig. 6E, represents the level of specular reflection from the metasurface, ξ_r, when illuminated normally. As is seen, at a resonance frequency of 8.08 GHz, the specular reflection is $\xi_r = -23.33$ dB, which corresponds to 0.5% of the incident power. This result additionally confirms that the normally illuminated metasurface reflects all the power at a desired angle of 70°. As seen from Fig. 6E, at frequencies below 7.2 GHz, where the metal strips on the substrate are weakly excited, the metasurface behaves as a usual mirror, obeying the simple reflection law.

DISCUSSION

We have demonstrated that by proper design of planar inhomogeneous low-loss reflectors, it is possible to realize conceptually perfect anomalous reflection, transforming a plane wave coming from an arbitrary direction into a single plane wave propagating into any other direction. Our approach fully removes the fundamental limitations on performance of known reflectarray antennas and known metasurfaces designed with the use of the generalized Snell's law. The active-lossy behavior of conceptually perfect anomalously reflecting metasurfaces, caused by power oscillations associated with the coexistence of two interfering plane waves in the same media, was realized with the use of carefully engineered effects of strong spatial dispersion in an inhomogeneous leaky-wave structure.

Although in this first demonstration we assumed that the incidence is a single plane wave, the power modulation appears also with more complex illuminations. Any arbitrary source and any metasurface response (desired reflected field) can be expressed in terms of plane wave expansions (19), and the superposition of those plane waves will require nonlocal response of the metasurface. However, the design methodology proposed in this study needs an optimization process for achieving the ideal performance. Despite the fact that the method has been successfully tested for different reflection scenarios (see section S2), the results significantly depend on structure optimization. In addition, one can expect that this dependence will increase with more complex field patterns. To simplify the optimization processes and reduce the simulation time, the interferences between all the elements of a unit cell should be modeled. This analysis could improve the design methodology and even avoid the use of optimization algorithms.

We hope that this research can open possibilities for the creation of various metasurfaces for shaping waves, such as holograms, focusing metasurfaces, or thin-sheet antennas, without losing power for parasitic scattering. In addition, the simple topology of metal patches printed on a thin dielectric substrate makes the proposed designs attractive in practical applications.

METHODS

Modeling of reflective metasurfaces based on the surface impedance

To verify the behavior of different reflective metasurfaces, we used numerical simulations in ANSYS Electromagnetics Suite 15.0.2 (HFSS 2014.0.2). The simulation domain is $D_x \times \lambda/10 \times 2\lambda$ (along the x, y, and z directions, respectively), and it corresponds to one period of the metasurface contained within master and slave boundaries in the x and y directions. The surface impedance was modeled as a piecewise constant using a discrete number of elements. Each element implements the impedance boundary dictated by Eqs. 1 to 3. The number of elements per period is 50 for the conventional design, 18 for the lossy, and 8 for the active design. The effect of the discretization was studied, and the number of elements was chosen to ensure the accuracy of the results. The system was illuminated by a TE-polarized plane wave. Two different simulations were done: plane wave excitation (extraction of the scattered fields; results represented in Fig. 2) and Floquet port excitation (study of the power scattered into each Floquet mode; results shown in Table 1).

For the inhomogeneous leaky-wave antenna surface (results shown in Fig. 3), the number of elements is 15. For the optimization process, we used the optimization tool of HFSS and the quasi-Newton (gradient) algorithm with the goal condition $S_{11} = 1$.

Design and modeling of a perfect reflectarray

The prototype presented in this work was designed for operation at 8 GHz. The unit cell consists of 10 rectangular copper patches above a copper ground plane. The width of all the patches is $w = 3.5$ mm. The thickness of the dielectric substrate is 1.575 mm, and final dimensions of each unit cell in the xy plane are $D_x = 40$ mm and $D_y = 18.75$ mm.

The first step in the design methodology was to determine the required reflected field for each element. To do that, we used the phase gradient defined by Eq. 3. Then, we periodically arranged each element (using a homogeneous array model) and calculated the length that produced the desired phase shift. The simulation domain was $D_x/10 \times D_y \times 2\lambda$ (along the x, y, and z directions). The dielectric material used in the simulations was Rogers 5880, with $\epsilon_r = 2.2$, tan $\delta = 0.0009$, and thickness = 1.575 mm. The rectangular patches and the ground plane were modeled as cooper ($\sigma = 58 \times 10^6$ S/m) with a thickness of 70 μm.

Once we knew the dimensions of all the elements in the unit cells, the second step was the optimization of the complete unit cell, which consists of 10 different patches. We did a numerical optimization of the structure that corrects the effects produced in the nonhomogeneous array that was not accounted for in the initial locally homogeneous approximation. The simulation domain of the complete unit cell was $D_x \times D_y \times 2\lambda$. The response of the inhomogeneous leaky-wave surface with 10 elements was optimized with HFSS. The quasi-Newton (gradient) algorithm was used, and the goal was defined as $S_{11} = 1$. The optimized dimensions of the patches are given in section S2B.

Perfect reflectarray realization and measurement

The metasurface sample designed to operate at a frequency of 8 GHz was manufactured using conventional printed circuit board technology on a 1.575-mm-thick Rogers 5880 substrate. The sample comprises 11 unit cells along the x axis and 14 unit cells along the y axis (Fig. 6A) and has the size of $11.7\lambda = 440$ mm and $7\lambda = 262.5$ mm, respectively.

The operation of the designed nonlocal reflecting metasurface was verified by measurements in an anechoic chamber emulating the free-space environment. A vector network analyzer was connected to a transmitting quad-ridged horn antenna with 11 dBi gain at 8 GHz (Fig. 6B). The metasurface was located at a distance of 5.5 m (about 147λ) from the transmitting antenna where the radiation from the antenna can be approximated as a plane wave. To control the metasurface orientation, it was attached to a platform rotating around the y axis. The receiving antenna, identical to the transmitting one, was positioned at a distance of 2.387 m (about 64λ) from the center of

the metasurface. Both antennas and the metasurface form in space a triangle with an angle of 70° at the metasurface center. The measured results are presented in section S2B.

SUPPLEMENTARY MATERIALS

Supplementary material for this article is available at http://advances.sciencemag.org/cgi/content/full/3/8/e1602714/DC1

section S1. Power modulation produced by reflective metasurfaces
section S2. Nonlocal perfect anomalous reflectors for different reflection angles
section S3. Analysis of the unit cell using two-dimensional evanescent fields
section S4. Scattered fields from a reference metal plate illuminated obliquely
section S5. Scattered fields from the normally illuminated metasurface
section S6. Correction factor for the signal amplitudes measured in the experiment
fig. S1. Total power density distribution for the conventional, lossy, and active designs (from left to right).
fig. S2. Initial approximation for nonlocal designs.
fig. S3. Real part of the scattered electric field when the designed metasurfaces are illuminated normally at $f = 8$ GHz.
fig. S4. Illustration of the desired performance of an ideally reflecting metasurface.
fig. S5. Real part of the total electric field.
fig. S6. Geometry of the problem with a metal plate.
fig. S7. Geometry of the problem with a metasurface.
table S1. Length of the strips, l, for different designs.
movie S1. Bandwidth analysis of conventional designs.
movie S2. Bandwidth analysis of nonlocal designs.

REFERENCES AND NOTES

1. J. Huang, J. A. Encinar, *Reflectarray Antennas* (Wiley, 2008).
2. D. Sievenpiper, L. Zhang, R. F. J. Broas, N. G. Alexopolous, E. Yablonovitch, High-impedance electromagnetic surfaces with a forbidden frequency band. *IEEE Trans. Microwave Theory Tech.* **47**, 2059–2074 (1999).
3. D. M. Pozar, Wideband reflectarrays using artificial impedance surfaces. *Electron. Lett.* **43**, 148–149 (2007).
4. S. B. Glybovski, S. A. Tretyakov, P. A. Belov, Y. S. Kivshar, C. R. Simovski, Metasurfaces: From microwaves to visible. *Phys. Rep.* **634**, 1–72 (2016).
5. N. Yu, P. Genevet, M. A. Kats, F. Aieta, J.-P. Tetienne, F. Capasso, Z. Gaburro, Light propagation with phase discontinuities: Generalized laws of reflection and refraction. *Science* **334**, 333–337 (2011).
6. S. Sun, K.-Y. Yang, C.-M. Wang, T.-K. Juan, W. T. Chen, C. Y. Liao, Q. He, S. Xiao, W.-T. Kung, G.-Y. Guo, L. Zhou, D. P. Tsai, High-efficiency broadband anomalous reflection by gradient meta-surfaces. *Nano Lett.* **12**, 6223–6229 (2012).
7. A. Pors, M. G. Nielsen, R. L. Eriksen, S. I. Bozhevolnyi, Broadband focusing flat mirrors based on plasmonic gradient metasurfaces. *Nano Lett.* **13**, 829–834 (2013).
8. A. Pors, S. I. Bozhevolnyi, Plasmonic metasurfaces for efficient phase control in reflection. *Opt. Express* **21**, 27438–27451 (2013).
9. M. Farmahini-Farahani, H. Mosallaei, Birefringent reflectarray metasurface for beam engineering in infrared. *Opt. Lett.* **38**, 462–464 (2013).
10. M. Esfandyarpour, E. C. Garnett, Y. Cui, M. D. McGehee, M. L. Brongersma, Metamaterial mirrors in optoelectronic devices. *Nat. Nanotechnol.* **9**, 542–547 (2014).
11. M. Kim, A. M. H. Wong, G. V. Eleftheriades, Optical Huygens' metasurfaces with independent control of the magnitude and phase of the local reflection coefficients. *Phys. Rev. X* **4**, 041042 (2014).
12. M. Veysi, C. Guclu, O. Boyraz, F. Capolino, Thin anisotropic metasurfaces for simultaneous light focusing and polarization manipulation. *J. Opt. Soc. Am. B* **32**, 318–323 (2015).
13. Z. Li, E. Palacios, S. Butun, K. Aydin, Visible-frequency metasurfaces for broadband anomalous reflection and high-efficiency spectrum splitting. *Nano Lett.* **15**, 1615–1621 (2015).
14. V. S. Asadchy, M. Albooyeh, S. N. Tcvetkova, A. Díaz-Rubio, Y. Ra'di, S. A. Tretyakov, Perfect control of reflection and refraction using spatially dispersive metasurfaces. *Phys. Rev. B* **94**, 075142 (2016).
15. N. M. Estakhri, A. Alù, Wave-front transformation with gradient metasurfaces. *Phys. Rev. X* **6**, 041008 (2016).
16. M. Collischon, H. Haidner, P. Kipfer, A. Lang, J. T. Sheridan, J. Schwider, N. Streibl, J. Lindolf, Binary blazed reflection gratings. *Appl. Opt.* **33**, 3572–3577 (1994).
17. P. Lalanne, S. Astilean, P. Chavel, E. Cambril, H. Launois, Blazed binary subwavelength gratings with efficiencies larger than those of conventional échelette gratings. *Opt. Lett.* **23**, 1081–1083 (1998).
18. A. Epstein, G. V. Eleftheriades, Synthesis of passive lossless metasurfaces using auxiliary fields for reflectionless beam splitting and perfect reflection. *Phys. Rev. Lett.* **117**, 256103 (2016).
19. A. Epstein, G. V. Eleftheriades, Passive lossless Huygens metasurfaces for conversion of arbitrary source field to directive radiation. *IEEE Trans. Antennas Propag.* **62**, 5680–5695 (2014).
20. S. Sun, Q. He, S. Xiao, Q. Xu, X. Li, L. Zhou, Gradient-index meta-surfaces as a bridge linking propagating waves and surface waves. *Nat. Mater.* **11**, 426–431 (2012).
21. G. Zheng, H. Mühlenbernd, M. Kenney, G. Li, T. Zentgraf, S. Zhang, Metasurface holograms reaching 80% efficiency. *Nat. Nanotechnol.* **10**, 308–312 (2015).

Citation: A. Díaz-Rubio, V. S. Asadchy, A. Elsakka, S. A. Tretyakov, From the generalized reflection law to the realization of perfect anomalous reflectors. *Sci. Adv.* **3**, e1602714 (2017).